Sensitivity of Basinwide Meridional Overturning to Diapycnal Diffusion and Remote Wind Forcing in an Idealized Atlantic–Southern Ocean Geometry

BARRY A. KLINGER*

Nova Southeastern University Oceanographic Center, Dania Beach, Florida

SYBREN DRIJFHOUT

Royal Netherlands Meteorological Institute (KNMI), De Bilt, Netherlands

JOCHEM MAROTZKE

School of Ocean and Earth Science, Southampton Oceanography Centre, Southampton, United Kingdom

JEFFERY R. SCOTT

Massachusetts Institute of Technology, Cambridge, Massachuselts

(Manuscript received 21 August 2001, in final form 29 July 2002)

ABSTRACT

Recent numerical experiments indicate that the rate of meridional overturning associated with North Atlantic Deep Water is partially controlled by wind stress in the Southern Ocean, where the zonal periodicity of the domain alters the nature of the flow. Here, the authors solve the cubic scale relationship of Gnanadesikan to find a simple expression for meridional overturning that is used to clarify the relative strength of the wind-forced component. The predicted overturning is compared with coarse-resolution numerical experiments with an idealized Atlantic Ocean–Southern Ocean geometry. The scaling accurately predicts the sensitivity to forcing for experiments with a level model employing isopycnal diffusion of temperature, salinity, and ''layer thickness.'' A layer model produces similar results, increasing confidence in the numerics of both models. Level model experiments with horizontal diffusivity have similar qualitative behavior but somewhat different sensitivity to forcing. The paper highlights the difference in meridional overturning induced by changes in wind stress or vertical diffusivity. Strengthening the Southern Ocean wind stress induces a circulation anomaly in which most of the water is subducted in the Ekman layer of the wind perturbation region, follows isopycnals down into the thermocline, and changes density again when the isopycnals near the surface in the Northern Hemisphere. Approximating the circulation anomaly by this subduction route allows for a surprisingly accurate prediction of the resulting heat transport anomaly, based on the surface temperature distribution. Some of the induced flow follows a second, near-surface northward route through low-latitude water that is lighter than the subducted flow. Overturning anomalies far from the wind stress perturbations are not completely determined by wind stress in the zonally periodic Southern Ocean: wind stress outside the periodic region strongly influences the transport of heat across the equator primarily by changing the temperature of the flow across the equator.

1. Introduction

Toggweiler and Samuels (1995, 1998) introduced the radical idea that a substantial part of the ''thermohaline circulation'' may in fact be driven by wind stress. Since there cannot be a net meridional geostrophic flow at any latitude and depth at which there are no zonal boundaries, they argue that the northward Ekman transport in the Southern Ocean must return below the sill depth of Drake Passage, about 2500 m. The northward surface Ekman transport then connects to the southward deep geostrophic flow via a sinking in the northern North Atlantic, where the stratification is weak enough to allow significant deep water formation. This North Atlantic Deep Water (NADW) cell is thus driven by both the classical interior diapycnal mixing (see for instance Bryan 1987) and by the strength of the southern wind.

Recently, Gnanadesikan (1999, henceforth G99) proposed a scaling for the strength of the NADW cell as

* Current affiliation: George Mason University, Fairfax, Virginia, and Center for Ocean–Land–Atmosphere Studies, Calverton, Maryland.

Corresponding author address: Dr. Barry A. Klinger, Center for Ocean–Land–Atmosphere Studies, 4041 Powder Mill Road, Suite 302, Calverton, MD 20705-3106.
E-mail: klinger@cola.iges.org

a function of vertical diffusivity κ_V, Southern Ocean windstress τ_S, and eddy thickness diffusivity κ_I (Gent and McWilliams 1990). We extend this work in several directions. The Gnanadesikan scaling consists of a cubic equation whose solution is not apparent by inspection. Since part of the appeal of scaling rules is to provide an easily understandable grasp of quantitative relationships, it would be useful to find an explicit formula relating overturning properties to forcing and other external parameters. After nondimensionalizing the system, we show that the cubic has a simple approximate solution that can be used to obtain better intuition about the physical system (section 2 below).

Gnanadesikan tested the scaling with a series of global, coarse-resolution numerical experiments with isopycnal mixing and thickness diffusion. We do a direct comparison of otherwise identical runs using the two common mixing schemes, horizontal (H) and isopycnal/Gent–McWilliams (GM). These numerical experiments use the GFDL Modular Ocean Model, which has fixed vertical levels. We also test these results with an isopycnal layer model (I), which allows for a numerically cleaner representation of isopycnal mixing. While other studies have examined differences between general circulation models using the different eddy parameterizations (Danabasoglu et al. 1994; Danabasoglu and McWilliams 1995; Hirst and McDougall 1998), these did not explicitly look at NADW cell sensitivity to different forcing. Our configuration is simpler than the global configuration of Gnanadesikan and others, consisting of a single basin in which the zonal boundaries are replaced by periodic boundary conditions in the latitude range of the Southern Ocean, a region we refer to as the ''channel.''

Toggweiler and Samuels' explanation of how windstress over the Southern Ocean influences the NADW cell focused on the influence of the periodic channel, which is in the vicinity of 55°S. This picture was based on numerical experiments that compared runs with wind altered in the wider latitude range south of 30°S [as was the case for McDermott (1996) and G99]. In contrast, the numerical experiments of Tsujino and Suginohara (1999) showed that adding wind to one hemisphere enhanced the deep thermohaline cell across much of the domain in a basin with no periodic channel at all. Tsujino and Suginohara's results raise the question of whether it is not merely the wind in Drake Passage latitudes that affects the NADW cell, but wind equatorward of the passage as well. More fundamentally, the closed-basin experiments raise the question of whether we understand what determines how much of subpolar meridional Ekman transport can be returned ''locally'' (within the subpolar region near the forcing) and how much must make a basinwide circuit. We conduct further sensitivity experiments to explore how much of the ''Drake Passage effect'' is really due to wind in Drake Passage.

The strengthening of the NADW cell by the wind in the Southern Ocean introduces a fundamental asymmetry between the northern and southern heat transport, with the ocean driving northward heat transport in both hemispheres. Since the heat transport is a key variable in ocean–atmosphere interaction, it is useful to be able to predict the size of this asymmetric component. Our single basin study has several components—including thermohaline overturning, wind stress forcing, and the influence of the channel—which contribute to the heat transport. We analyze the heat transport in terms of the individual components, especially the influence of wind stress poleward of latitude 30° on the heat transport.

2. Scaling for southern winds and uniform diapycnal diffusion

Gnanadesikan added the classical ''advective–diffusive'' overturning (Bryan and Cox 1967; Bryan 1987; Colin de Verdiere 1988) to a component driven by Southern Ocean Ekman transport and retarded by Southern Ocean lateral eddy fluxes. He assumed that the total North Atlantic overturning cell was the sum of the Southern Ocean overturning and the diffusively driven overturning, to derive a cubic equation in pycnocline thickness D:

$$\left(\frac{c\Delta b}{f_0}\right)D^3 + \left(\kappa_I\frac{L_x}{L_y}\right)D^2 - \left(\frac{\tau L_x}{\rho f_S}\right)D - \kappa_V A = 0. \quad (1)$$

Here Δb is the pole-to-equator range of surface buoyancy ($=g\Delta\rho/\rho$, for gravitational acceleration g, density range $\Delta\rho$, and density ρ); f_0 and f_S are values of the Coriolis parameter at midlatitude and in the Southern Ocean, respectively; κ_I is the thickness diffusivity; L_y is the width of the Southern Ocean frontal zone; L_x is the zonal length of the Southern Ocean; τ is the Southern Ocean wind stress; A is upwelling area (presumably most of the basin), and c is a constant explained below. Total NADW cell volume transport, T_N, can be related to D via geostrophy, which implies that

$$T_N = c\Delta bD^2/f_0. \quad (2)$$

The meridional transport is directly related to the *zonal* buoyancy difference rather than Δb, but there is reason to believe that the two buoyancy scales are proportional, with a proportionality constant c (Park and Bryan 2000; Marotzke 1997). Gnanadesikan's scaling was explicitly based on western boundary current dynamics but resulted in essentially the same relation as (2). It should be noted that using the same scale vertical length scale D for horizontal velocity [Eq. (2)] and pycnocline depth is problematical (Scott 2000), and that overturning strength also depends on interhemispheric density differences (Rahmstorf 1996; Klinger and Marotzke 1999; Marotzke and Klinger 2000) but here we will follow G99's scaling.

In the case of no wind and no thickness diffusion (τ

TABLE 1. Scaling for numerical experiments for low and high winds [κ_V: cm^2 s^{-1}; T_0 and T_N: Sv; D_0: m; S, E, and d: nondimensional; d is calculated from (11), and T_N from (9)].

				E		d		T_N	
κ_V	T_0	D_0	S	Low	High	Low	High	Low	High
				Default basin					
0.05	4.1	91	0.095	0.55	1.6	1.12	1.43	5.2	8.3
0.50	19.0	195	0.044	0.35	1.0	1.02	1.09	19.8	22.5
				Wide basin					
0.05	10.3	144	0.24	0.87	2.6	1.17	1.63	14.1	27.6
0.50	48.0	310	0.11	0.19	0.56	1.02	1.12	50.0	60.6

$= 0$ and $\kappa_I = 0$), we recover the classical advective–diffusive relationships from (1):

$$D_0 = \left(\frac{\kappa_V A f_0}{c\Delta b}\right)^{1/3} \tag{3}$$

and, inserting (3) into (2),

$$T_0 = (c\Delta b \kappa_V^2 A^2 / f_0)^{1/3}. \tag{4}$$

Nondimensionalizing (1) reduces the number of variables and makes it somewhat easier to see patterns in the solution. There are many possible sets of quantities to use as scales, but D_0 and T_0 stand out as being especially familiar quantities. Then we can define $d = D/D_0$, a measure of how different the pycnocline depth is from its classical value (at $d = 1$), and (1) becomes

$$d^3 + Sd^2 - Ed - 1 = 0. \tag{5}$$

Here the wind strength is given by

$$E = \frac{\tau L_x/\rho f_S}{T_0} = \frac{\text{Ekman transport}}{\text{classical diffusive transport}} \tag{6}$$

and the strength of horizontal eddy mixing is given by

$$S = \frac{L_x}{L_y}\frac{\kappa_I/A}{\kappa_V/D_0^2}, \tag{7}$$

which does not have as straightforward a physical interpretation as E. However, we can define a meridional length scale M such that $A = L_x M$, in which case,

$$S = \frac{D_0^2/\kappa_V}{L_y M/\kappa_I}. \tag{8}$$

This can be interpreted as a ratio of timescales for vertical and lateral diffusion. Using the above scaling, we can also define a nondimensional cell strength $t_N = T_N/T_0$. From (2), (3), and (4), this becomes

$$t_N = d^2. \tag{9}$$

For small E and S, a first-order perturbation solution to (5) around $d = 1$ yields

$$d \approx 1 + (1/3)(E - S). \tag{10}$$

Equation (5) can be solved numerically. We choose the parameter range $0 < S < 1$ and $0 < E < 6$. Parameter values too large for this range occur as $\kappa_V \to 0$, in which case the classical scaling does not provide convenient scales for nondimensionalization and nondimensionalization should be based on the wind-driven limit instead. As we will see, our numerical experiments stay inside this range even for κ_V as low as 0.05 cm^2 s^{-1}. Within this range, we find that the contours of $d(E, S)$ are well approximated by straight lines. Using this fact and doing some empirical curve fitting, we find that the approximation

$$d = \frac{1 + 0.28E - 0.055S}{1 + 0.22S} \tag{11}$$

is within 0.05 of the exact solution in this parameter range. Note that (11) is fairly close to the perturbation solution (10).

Table 1 displays the key dimensional and nondimensional parameters discussed above for several values of κ_V, τ, and basin width corresponding to the numerical experiments described in the next two sections. Low and high wind cases have τ of 0.06 and 0.18 N m^{-2}, respectively, corresponding to 0.5 and 1.5 times observed Southern Hemisphere maximum westerlies. The zonally periodic channel is assumed to be at 50°S (see next section). Default and wide basin widths are 60° and 240° longitude, respectively. Basin lengths (for calculating A) are 120° latitude and $L_y = 1000$ km. Surface buoyancy range is 0.05 m s^{-2} (similar to the real world), $c = 1$, and $\kappa_I = 1000$ m^2 s^{-1}, a value typical for coarse-resolution numerical models and perhaps the right order of magnitude for parameterizing mesoscale eddies in the real world.

For these values, Table 1 shows that S (a measure of the importance of κ_I) is small in all cases but not negligible for low κ_V and wide basin. The Southern Ocean Ekman transport can be smaller or larger than T_0 (as measured by E), for various combinations of τ and κ presented here. We can see from d (or by comparing T_N to T_0) that the total overturning is not very sensitive to τ if $\kappa_V = 0.5$ cm^2 s^{-1} but is quite sensitive for $\kappa_V = 0.05$ cm^2 s^{-1}. The actual value of κ_V in the ocean is rather poorly constrained and geographically nonuniform, ranging from $O(0.1$ cm^2 s$^{-1})$ in the thermocline to $O(1.0$ cm^2 s$^{-1})$ in abyssal water (Gregg 1987; Ledwell et al. 1993; Toole et al. 1997; Polzin et al. 1997).

What is the relative importance of the classical component due to vertical diffusion and the wind-driven component of the meridional overturning? In view of the observational uncertainties, we pose the question another way. The wind contribution grows in importance as τ increases and as κ_V and κ_I decrease. Given τ in the Southern Ocean, how weak would κ_V have to be in order for the actual overturning to be at least twice as large as T_0? To estimate this, we first invert (11) to find $E(S)$ for a given $d^2 = t_N$. We do not know what S should be, but guided by the results in Table 1, we set $S = 0.1$ [for which $E(S) = 1.5$]; results are not very sensitive to S. In the real world, at 58°N, at the latitude of Drake Passage, $\tau \approx 0.085$ N m^{-2} (Hellerman and Rosenstein 1983) over a zonal distance of 360°, which produces an Ekman transport T_E of 14 Sv (Sv $\equiv 10^6$ m^3 s^{-1}). Note that in numerical models Drake Passage's northern edge is usually further north, where T_E is larger because windstress, zonal width, and $1/f$ are all larger. For calculating T_0, the relevant area of the World Ocean is roughly equal to that of a sector about 240° wide. Since $E = T_E/T_0$, we use (4) to find the κ_V which results in the desired E and T_E. For $d^2 \geq 2$ (i.e., for wind to at least double the thermohaline upwelling), $E \geq 1.6$ and $\kappa_V \leq 0.04$ cm^2 s^{-1}, while for $d^2 \geq 1.5$, $E \geq 0.9$ and $\kappa_V \leq 0.09$ cm^2 s^{-1}. This rough estimate indicates that globally averaged κ_V may need to be on the low side of observational estimates for the meridional overturning to be dominated by southern wind.

3. Numerical models

Two different primitive equation numerical models are used. One is the Geophysical Fluid Dynamics Laboratory Modular Ocean Model (MOM) version 2.2 (Pacanowski 1996), in spherical coordinates in the horizontal and constant-depth coordinates in the vertical. The second model is based on the code of Bleck and Boudra (1986) and discretizes the vertical into constant-density layers.

a. Level model

The basin is a sector that ranges from 66°S to 62°N (measuring from the centers of temperature grid cells), is 60° wide, and is 4500 m deep. There are 16 vertical levels ranging in thickness from approximately 52 m at the top to approximately 510 m at the bottom. The default horizontal gridspacing is 2° in both horizontal directions; some sensitivity tests have 1° resolution and others have 4° in latitude and 3.75° in longitude. The appendix discusses resolution sensitivity. From 64°S to 48°S (measuring from the centers of temperature grid cells) the basin is periodic in longitude, thus representing the topology of the Southern Ocean. We refer to this area as the channel. Because the zonal boundaries in MOM are generated by filling grid-cells with ''land,'' the channel has an extra 2° of width, which is given a depth of about 2545 m. This ridge in the model's ''Drake Passage'' represents the ridge at the eastern edge of the Scotia Sea, which in the real ocean is somewhat to the east of Drake Passage. The model channel is simpler and wider than the Drake Passage region in the real world, which has land north of about 55°S as well as the South Sandwich Islands emerging from the ridge to its east. These approximations are appropriate to the coarse resolution of the model.

Our ''twin'' experiments have different forms for lateral diffusion of temperature T and salinity S. In ''H'' experiments, T and S are simply diffused horizontally ($\kappa_H = 1000 \times 10^4$ cm^2 s^{-1}). In ''GM'' experiments, T and S are diffused along isopycnals. In addition, the model calculates a ''bolus'' velocity that is added to the traditional velocity components. This velocity parameterizes correlations between eddy variability in density and in velocity (unresolved by the model) and is equivalent to the lateral diffusion of ''thickness,'' $d\rho/dz$, where z is the vertical coordinate (Gent and McWilliams 1990). In GM runs, lateral diffusion of T, S, and thickness are all $\kappa_I = 1000 \times 10^4$ cm^2 s^{-1}, the full diffusivity tensor is used rather than a small-angle approximation. Both H and GM runs also have horizontal viscosity $\nu_H = 250\,000 \times 10^4$ cm^2 s^{-1} (giving a western boundary current width appropriate to the coarse resolution) and vertical viscosity $\nu_V = 100$ cm^2 s^{-1}. Different experiments have ''high'' vertical diffusivity of $\kappa_V = 0.5$ cm^2 s^{-1} and ''low'' diffusivity of $\kappa_V = 0.05$ cm^2 s^{-1}. The basin walls and bottom have insulating and no-slip boundary conditions. In all experiments, the advective terms in the model's temperature and salinity evolution equations use the flux-corrected transport scheme, which is a compromise between the overly diffusive upstream difference scheme and the property-altering centered difference scheme (Gerdes et al. 1991).

Surface level T and S are strongly restored to zonally uniform reference profiles with a restoring timescale of 30 d. The behavior of the circulation can be different when a weaker restoring is used (Rahmstorf and England 1997). The different behavior occurs because changing the wind stress changes the surface temperature distribution which in turn affects the meridional overturning. Here we examine the response given strongly constrained temperature; given the rules relating wind forcing to temperature response, the results here can be extended to a more realistic situation when the relationship between wind forcing and surface temperature variation is clarified, which is beyond the scope of the present work. The reference profiles are symmetric about the equator and loosely based on realistic SST and SSS profiles for the ocean:

$$T_R = 28\{0.5[1 + \cos(\pi\phi/68)]\}^{3/4}, \qquad (12)$$

where ϕ is latitude (in degrees), and

$$S_R = 34 + 4.125e^{-(\phi/25)^2}\sin(\pi\phi/50)^2, \quad (|\phi| < 50) \tag{13a}$$

$$S_R = 34, \quad (|\phi| > 50) \tag{13b}$$

(see Fig. 1a). In all experiments, density is calculated via an approximation to the standard nonlinear equation of state. The surface density based on T_R and S_R is shown in Fig. 1b.

The model is also driven by zonally uniform zonal wind stress. The profiles are based on the smoothed, annually and zonally averaged Hellerman and Rosenstein (1983) data. South of 30°S, the ''weak wind'' case has windstress multiplied by 0.5, while the ''strong wind'' case has wind stress multiplied by 1.5 (Figs. 1c,d). Experiments with low diffusivity and each of the two wind strengths were also conducted in a wider basin, 240° longitude wide. The larger basin surface area and Southern Ocean zonal extent are more like the real world than the narrow-basin experiments and provide a larger wind- and buoyancy-driven overturning signal with which to test the scaling.

Further wind-sensitivity experiments are conducted with ''northern winds'' and ''channel winds.'' For the northern winds experiment, wind stress $\tau_S(\phi)$ is identical to the strong wind except north of 30°N, which has an anomaly equal to the difference between strong (τ_S) and weak (τ_W) winds (Figs. 1c,d), so that for $\phi > 30°$,

$$\tau_N(\phi) = \tau_S(\phi) + (\tau_S(-\phi) - \tau_N(-\phi)). \tag{14}$$

The channel winds experiment is similar to the strong winds experiment but with the strengthened winds confined to the channel and poleward (Figs. 1c,d):

$$\tau_C(\phi) = \tau_W(\phi) + (\tau_S(\phi) - \tau_W(\phi))W(\phi), \tag{15}$$

where $W = 1.0$ for $\phi \le -51°$, $W = 0.0$ for $\phi \ge -45°$, and W varies linearly between 45°S and 51°S.

In each experiment, the system is integrated forward in time until the trend in peak meridional overturning is small (typically no more than 0.01 Sv century^{-1}) and decreasing. Unequal time steps are taken for the momentum (1 h) and temperature and salinity (typically 5 days) evolution equations, as described by Bryan (1984). The approach to equilibrium is further accelerated by occasionally extrapolating exponentially decaying trends in temperature and salinity (Klinger 2000). Typical integration times were 1000 to 5000 years as measured by the temperature evolution equation.

b. Isopycnal model

The domain of the model, bottom topography and resolution are as in the level model, as is the isopycnal and vertical diffusion, horizontal viscosity, and lateral thickness diffusion. The isopycnal model omits vertical viscosity (see Bleck and Boudra 1986) and has a linear equation of state. There are 36 isopycnal layers.

The present model is an extension of the model described in Drijfhout (1994). It is better suited to our idealized study than more recent versions of the model (MICOM) in which features necessary for realistic, high-resolution simulations of the ocean increase the computational cost and programming complexity of the model. It contains more vertical resolution and diapycnal diffusion according to Huang and Bryan (1987). Splitting between barotropic and baroclinic mode is according to Bleck and Smith (1990). The model takes unequal time steps in momentum and density (Bryan 1984) as with the level model. The wind stress is assumed to decrease linearly within a layer of 50 m, and the bottom stress decreases linearly within a layer of 25 m. The treatment of buoyancy forcing follows the methodology described in Drijfhout (1994). Both models are driven by equivalent wind and buoyancy forcing.

The level model relaxes both temperature and salinity to prescribed SST and SSS profiles with a restoring timescale of $t_R = 30$ days. This is equivalent to restoring density to the profile shown in Fig. 1b with $t_R = 30$ days. The layer model directly relaxes density with a restoring timescale of 30 days to the profile shown in Fig. 1b. To calculate the buoyancy flux through the surface we use the layer-weighted density of the upper 50 m for restoring. This buoyancy flux is used to drive a mass exchange between the surface layer (the first layer containing mass) and the layer below. The increase/decrease of the surface layer, Δh is given by

$$\Delta h = \frac{50\Delta t(\rho_s - \rho_*)}{t_R\Delta\rho}, \tag{16}$$

where Δt is the model timestep, ρ_s is the layer weighted density of the upper 50 m, ρ_* is the reference density for restoring, and $\Delta\rho$ is the density difference between surface layer and layer below.

If Δh is negative and larger than the thickness of the surface layer, the remaining part of the buoyancy flux is used for mass exchange between the two uppermost subsurface layers (when present). If Δh is positive and there is a massless layer with density larger than the reference density, then the buoyancy flux is used to fill up this massless layer. The mass exchange due to diapycnal diffusion is applied after the mass exchange due to surface buoyancy gain/loss. Momentum is exchanged between layers, consistent with this mass exchange. The runs have been integrated for 1500 years. At the end of the integration the trend in the stratification is small and decreasing at a rate such that the streamfunction values at year 1500 are likely to be within 1% of their final values.

4. Overturning in numerical experiments

The meridional overturning streamfunction Φ_z, based on the zonal integral of meridional velocity v at every depth z, does not highlight the water mass transformation. An alternative streamfunction, Φ_ρ can be com-

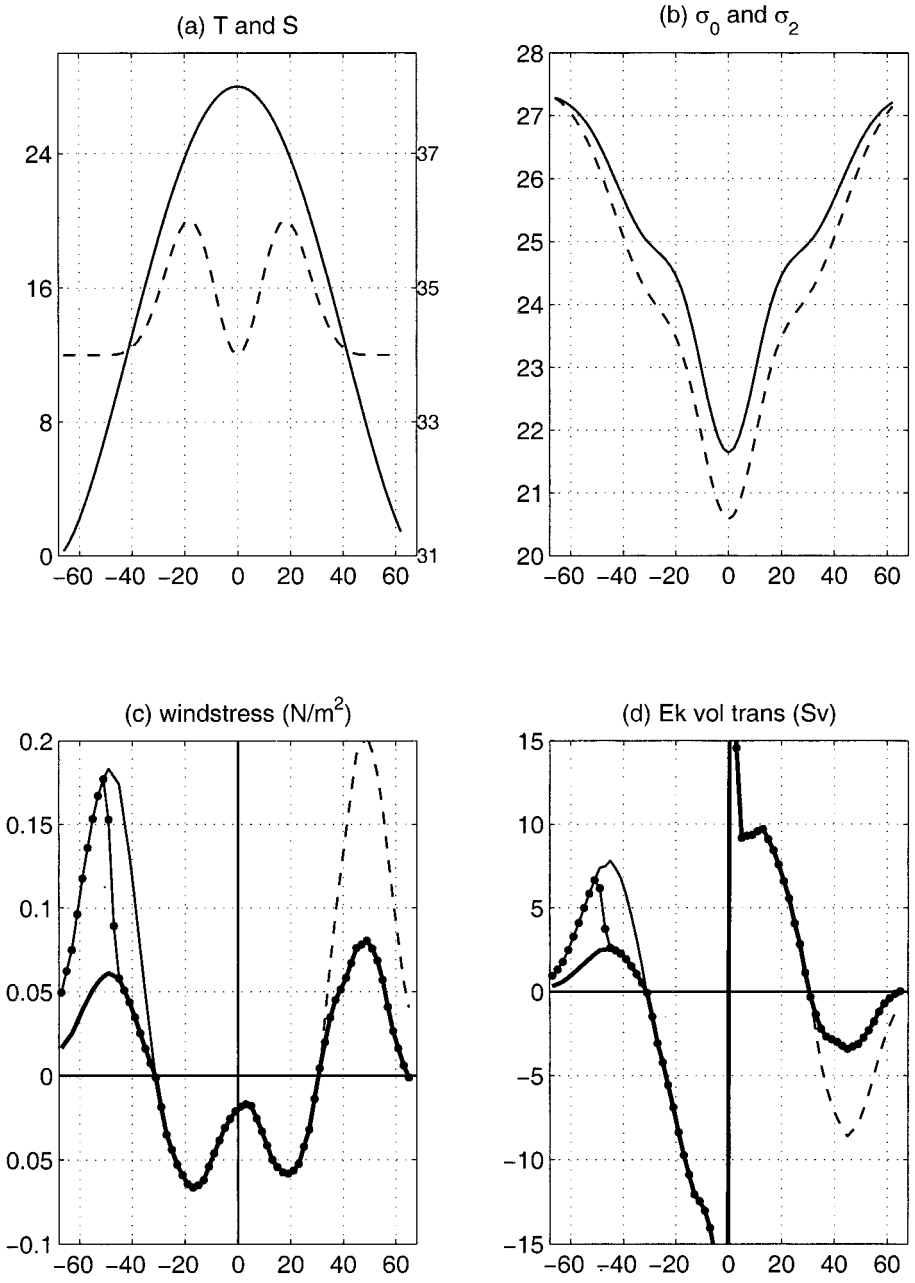

FIG. 1. Surface forcing as a function of latitude for experiments. Restoring profiles for (a) temperature (solid, left axis labels) and salinity (dashed, right axis labels) and (b) density as measured by σ_0 (solid) and σ_2 (dashed, offset by 9.3115 kg m^{-3}). (c) Zonal wind stress for weak wind (heavy solid), strong southern wind (solid), strong channel wind (solid with dots), and strong northern and southern wind (dashed). (d) Meridional Ekman volume transport; same line styles as in (c).

puted by taking the zonal integral of v at constant density so that ''vertical'' flow in the ρ–ϕ plane can be interpreted as net cross-isopycnal flow. In the GM experiments, one can also look at advective, eddy (refering to the bolus velocity that parameterizes eddy-induced transport unresolved by the model) or total (advective plus eddy) components of velocity. In the discussion below, ''overturning'' will refer to Φ_ρ (including eddy component for the GM experiments) unless noted otherwise. Here Φ_ρ is calculated on σ_2 surfaces. In theory one should use neutral surfaces instead (McDougall 1987; Hirst et al. 1996), but in practice this is only an important issue when there are large S gradients on T surfaces, which is not the case over most of the domain in our experiments. Calculating Φ_ρ on σ_0 surfaces for the strong wind, high κ_V case gives nearly identical results.

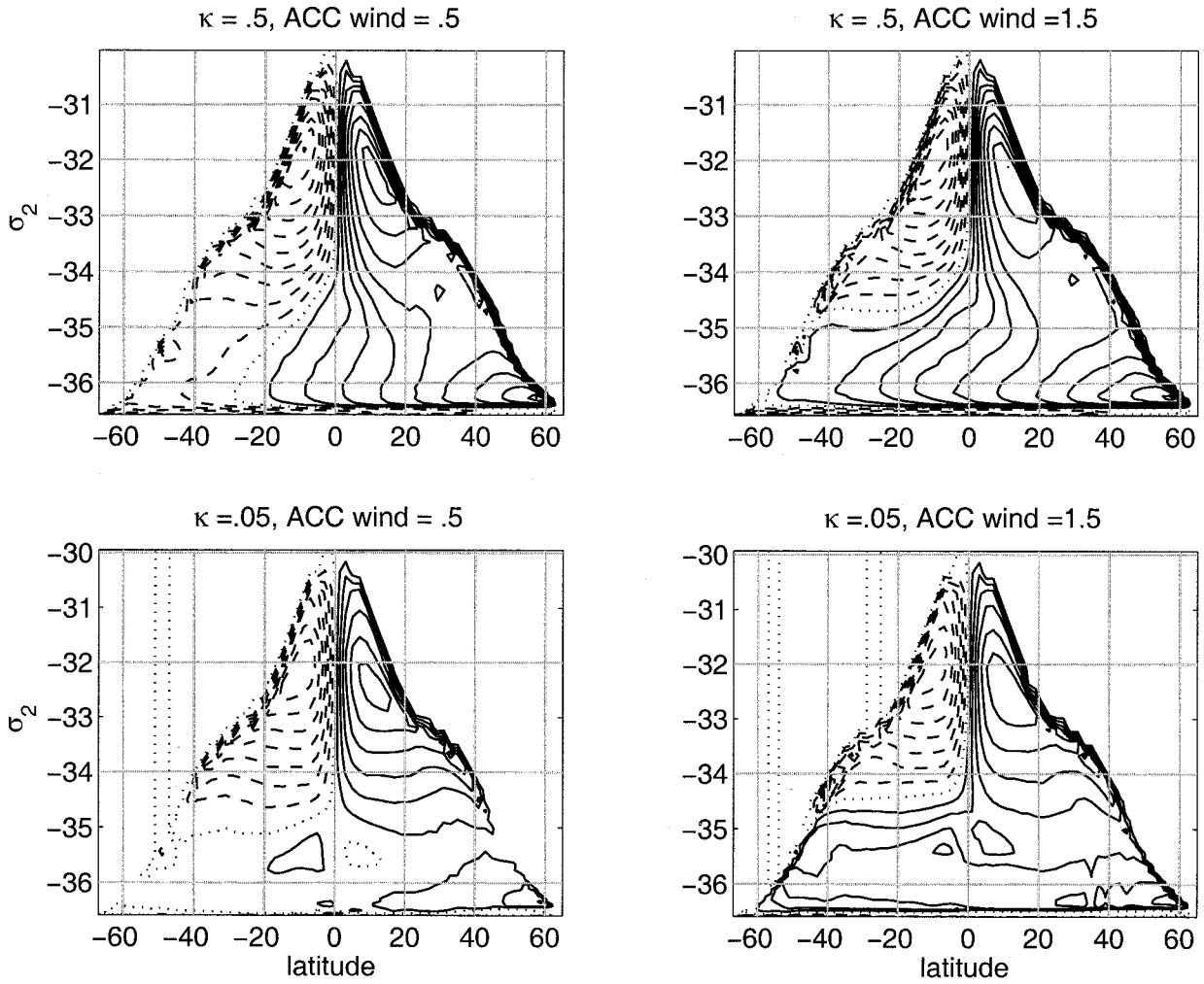

FIG. 2. Meridional overturning for low and high vertical diffusivity κ_V and low and high southern wind τ, GM runs including both advective and eddy components. Contour interval = 1 Sv. Overturning with σ_2 coordinate is calculated using 51 unequally spaced density intervals that give higher resolution for higher σ_2. In all overturning figures, northern sinking cells are solid, southern sinking cells are dashed, and zero-contours are dotted.

All numerical experiments have an NADW cell consisting of sinking near the northern boundary, dense southward flow, and return flow closer to the surface (Fig. 2). Note that surface zonal density variations are small (due to the coarse resolution and strong restoring); only streamlines in the lightest water at each latitude represent surface flow. Overturning streamfunctions are qualitatively similar for GM (Fig. 2), H (not shown), and layer model (Fig. 3) experiments. Shallow ''subtropical cells'' (McCreary and Lu 1994), driven by poleward Ekman transport, dominate the lightest water. There is generally some sign of an abyssal counterrotating ''AABW cell'' (Antarctic Bottom Water), which is barely visible in the Φ_ρ figures. The NADW cell grows stronger when either τ or κ_V are increased. In the weak wind cases, the NADW cell does not extend to near the southern boundary; a single southern-sinking cell consisting of a merged AABW cell and subtropical cell dominates the Southern Hemisphere. In the strong wind case, the northward Ekman transport south of 30°S extends the NADW cell to near the southern boundary.

It is not immediately clear from the $\Phi_\rho(\phi, \rho)$ contours (Figs. 2 and 3) how the flow depends on depth, as in traditional $\Phi_z(\phi, z)$ contours. For a more direct comparison to Φ_z, Φ_ρ can be mapped onto the (ϕ, z) plane. To do this, we invert the zonal-average density $\rho(\phi, z)$ so that for a given ϕ and ρ we can assign a corresponding z. The resulting streamlines (Figs. 4a,c) look like traditional z-coordinate overturning, but unlike a $\Phi_z(\phi, z)$ figure, the flow across an isopycnal gives a true measure of the cross-isopycnal flow. The apparent depth of a given $\Phi_\rho(\phi, \rho)$ streamline could differ somewhat from the actual depth of the flow if the bulk of the flow occurs at a longitude where the isopycnal depth is different from its zonal mean.

Comparison of $\Phi_z(\phi, z)$ and $\Phi_\rho(\phi, z)$ for the GM and

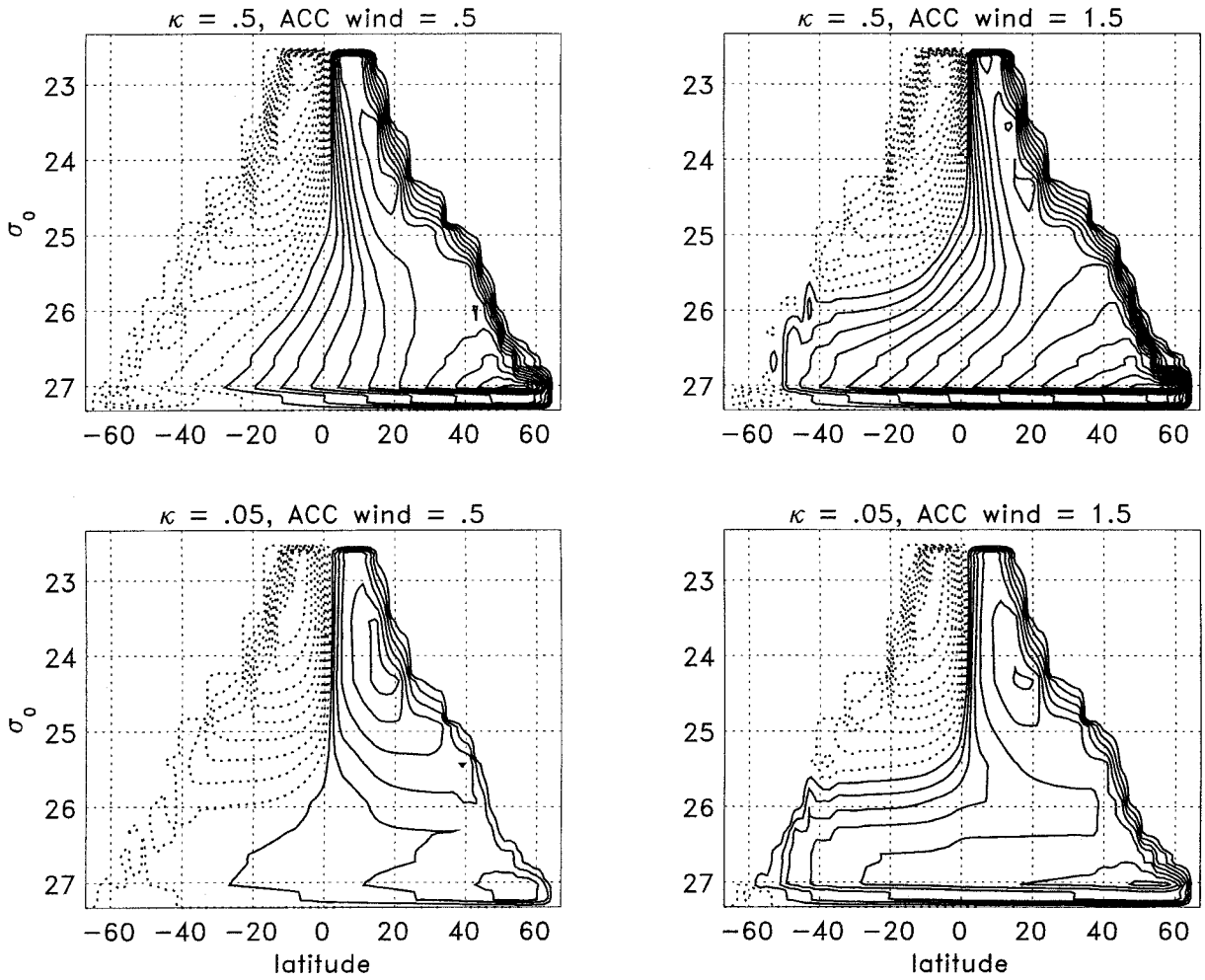

FIG. 3. As in Fig. 2 but for isopycnal model runs.

H (not shown) experiments with high κ_V and high τ (Fig. 4a,b) shows a NADW cell in all versions. The depth and strength of this cell is similar for $\Phi_\rho(\rho, z)$ and $\Phi_z(\rho, z)$, but other features vary. Within about 10° of the northern boundary, Φ_z shows a much stronger maximum than Φ_ρ, especially in the GM experiments. The discrepancy is related to the fact that isopycnals tilt sharply there, extending from the surface in the west down to below 1000 m in the east. Thus a given isopycnal includes northward flow near the surface and southward flow at depth, which tends to cancel each other in Φ_ρ. For the isopycnal model experiments, $\Phi_\rho(\phi, z)$ (Figs. 4c,d) shows that the NADW cell takes up more of the water column than in the GM case, with the AABW cell correspondingly reduced. This is probably due to the layer model replacing separate temperature and salinity fields with a single σ_0 field. The temperature and salinity of the AABW source water makes it denser than the NADW source water, but the density difference is at least twice as great for σ_2 to σ_4, which are the appropriate measures of density for AABW water in the level model, than for σ_0.

We characterize the strength of the NADW cell with a single volume transport representing the maximum Φ_ρ in a density range that excludes the subtropical cells. Each H experiment has overturning values about twice as great as the corresponding GM experiment (see Table 2 and appendix), which is a consequence of the generally greater diapycnal mixing associated with horizontal diffusion (Böning et al. 1995; Veronis 1975). The I experiments have somewhat smaller upwelling values than GM for low κ_V (Table 2), which may be due to larger numerical diffusivity in the GM experiments.

Qualitatively, our H, GM, and I experiments show similar variations with wind, vertical diffusivity, and basin width (Table 2). The H experiments are less sensitive to changes in κ_V than GM and I experiments. Presumably this is because the diapycnal diffusivity in the H experiments is equal to κ_V plus a significant contribution related to κ_H so that the fractional change in

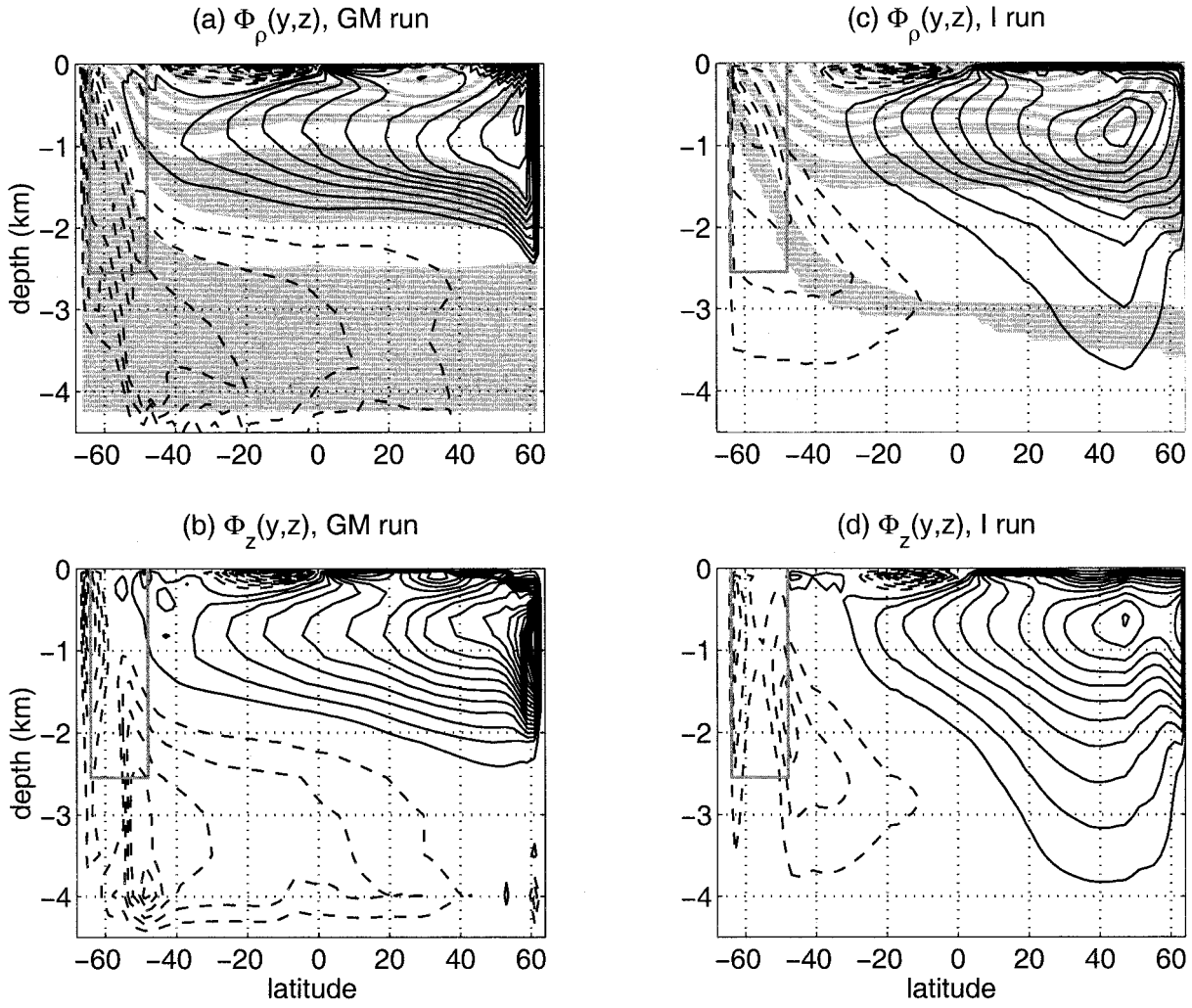

FIG. 4. Overturning streamfunction as a function of depth and latitude for integrations performed at (top) constant density and (bottom) constant z for high κ_V and high τ, (left) GM and (right) I. Contour interval is 1 Sv. In the upper panels, shading shows zonal average density (σ_2 for GM, σ_0 for I), with nonuniform contour intervals chosen to show details in both deep and shallow water. Contours are defined by making the transformation $s \equiv [(\sigma_M - \sigma_2)/(\sigma_M - \sigma_m)]^{1/2}$, where σ_M and σ_m are the maximum and minimum, respectively, values of σ_2. Contour interval in s is 0.05. The dark gray rectangle shows a region of zonal periodicity.

diapycnal diffusivity is less than the fractional change in κ_V. Sensitivity to wind stress is different in H than in GM and I, but not consistently larger or smaller.

Table 1 shows calculations of the nondimensional parameters and overturning prediction described in section 2, and Table 3 shows the model overturning values scaled by the predictions. To measure how well the scaling fits the experiments, we compare the variation in the raw data (excluding wide-basin experiments) to that of the same data normalized by the scaling. In the H

TABLE 2. Numerical experiment overturning strength for low and high winds: κ_V as in Table 1; all other numbers refer to maximum in NADW cell overturning streamfunction (Sv) calculated in density coordinate; for GM runs this is for total streamfunction (advective plus eddy terms).

	H (level model)		GM (level model)		Layer model	
κ_V	Low	High	Low	High	Low	High
0.05	6.6	10.6	3.1	5.5	2.1	4.2
0.50	13.6	18.4	9.2	11.1	9.1	10.7
			Wide basin, coarse resolution			
0.05	26.1	39.8	9.5	17.5		

TABLE 3. Nondimensional overturning from numerical experiments for low and high winds: κ_V as in Table 1; all other numbers are from Table 2 scaled by corresponding T_N from Table 1.

	H (level model)		GM (level model)		Layer model	
κ_V	Low	High	Low	High	Low	High
0.05	1.27	1.27	0.60	0.66	0.40	0.51
0.50	0.69	0.82	0.46	0.49	0.46	0.48
			Wide basin, coarse resolution			
0.05	1.85	1.44	0.67	0.64		

series, the unscaled NADW cell strengths (Table 2) have a standard deviation of about 40% of the average of all four experiments; for the GM series the standard deviation is 50% of the average. The normalized strengths have a standard deviation of 30% of the average for the H experiments and 16% of the average for the GM experiments (Table 3). Statistics for the layer model overturning are similar to the GM results, with G99's scaling reducing the scatter of the NADW strength from 62% of the average for the raw values to 10% for the scaled values (Table 3). In summary, the scaling collapses the data somewhat for H mixing, but it provides a much better fit to the GM and the best fit to the I cases. However, the sensitivity of the GM and I experiments to wind is somewhat greater than predicted by the scaling, while the sensitivity to κ_V is somewhat less than predicted (Table 3).

To save on computer time, wide-basin experiments are only conducted at coarse resolution, and so are not strictly comparable to the results from other experiments in Tables 2 and 3. However, from these tables we can see that in the wide basin, changing the wind makes an $O(10$ Sv) change in overturning for both H and GM mixing, and that the scaling provides a good fit to the GM case but not to the H case.

G99's scaling is partially based on the idea that the wind contribution to the NADW cell is simply the Ekman transport minus an eddy transport in the Southern Ocean. Consequently raising κ_I decreases the transport, as (11), (7), and (9) show. Does horizontal diffusivity κ_H play an analogous role in the H case? We conduct a strong wind H experiment with $\kappa_H = 250$ cm^2 s^{-1} rather than 1000 cm^2 s^{-1} to answer this question. The experiment is run at coarse resolution, with $\kappa_V = 0.05$ cm^2 s^{-1}, narrow basin, and all other parameters identical to the other experiments. Reducing κ_H in this way increases the NADW cell strength by 16%. According to (11), for these parameters, the transport should be about 6% larger if κ_I is reduced from 1000 to 250 cm^2 s^{-1}. Thus κ_H plays an analogous role to κ_I, but (as with other parameters) has quantitative differences from G99's scaling.

5. Anomalies associated with forcing perturbations

In the following discussion, we shift the focus to the anomalous meridional volume transport, heat transport, and velocity associated with changing κ_V or the windstress. These anomalies highlight the dynamics underlying the basic flow. In particular, we show in section 5a that varying the wind stress produces overturning anomalies that are approximately adiabatic by some integral measures, as implied by Toggweiler and Samuels (1995) and by the surface heat flux calculations of Hasumi and Suginohara (1999). This then allows us to produce a simple formula (section 5b), which describes the magnitude of the heat transport driven by westerlies. Finally, in section 5c we show that the westerlies actually drive significant diabatic flow anomalies in regions where integral measures imply that the flow anomaly is adiabatic. Throughout section 5, we highlight the different effects of wind stress anomalies in the channel region and outside the channel.

a. Meridional volume transport

The strength of the NADW cell is sensitive to both κ_V and τ, but the overturning anomaly associated with each is quite different.

Increasing κ_V increases the low- and midlatitude upwelling and has the strongest effect in the Northern Hemisphere (Fig. 5). Because the diapycnal diffusivity is increased, the circulation changes are associated with cross-isopycnal flow. Note that the geographic distribution of changes induced by changes in κ_V can be very different from the results shown here when κ_V is only changed within a restricted latitude band (Marotzke and Klinger 2000). The H and I overturning anomalies (not shown) are similar to the GM anomalies, but with greater magnitudes, less noise in the deep Φ_z, and (for H experiments) a deeper NADW anomaly. The Φ_z anomaly reveals a pattern similar to overturning in a basin with no wind stress, no channel, and surface density greater at the northern boundary than at the southern boundary. In that case, the lighter hemisphere contains a relatively shallow, ''subordinate'' cell above the analogue of the NADW cell (Cox 1989; Klinger and Marotzke 1999, among others). The channel and wind stress complicate the pattern when the full overturning (as opposed to the difference between experiments) is viewed. The subordinate cell merges with the subtropical cell in the weak wind cases (Fig. 2), and is eliminated by the enlarged NADW cell in the strong wind cases (Figs. 2 and 4).

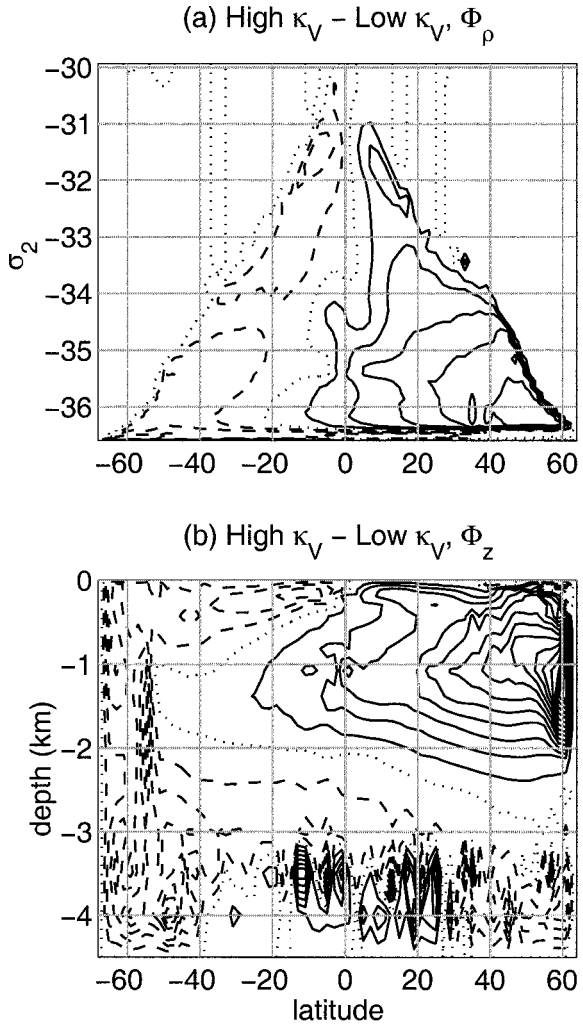

FIG. 5. Difference in (a) Φ_ρ and (b) Φ_z between high κ_V and low κ_V GM experiments. Both experiments have low τ. Contour interval is 1 Sv.

Increasing the wind south of 30°S creates overturning anomalies dominated by a basin-spanning cell with light water flowing north and dense water flowing south (Fig. 6). Most of the anomalous cross-isopycnal flow occurs near the surface. The anomalous circulation is about the same for the high κ_V case as for the low κ_V case (not shown). Since the wind anomaly is confined to the region south of 30°S, most of the anomalous density transformation occurs there as well as north of 30°N where the affected isopycnals outcrop. The overturning pattern shows some asymmetry with respect to the equator; this is particularly evident in the z-coordinate view, in which the northward flow anomaly is confined to the Ekman layer (i.e., the top level) in the Southern Hemisphere but spans the top 400 m in the Northern Hemisphere. The H and layer model cases (not shown) are similar, but with larger and (for H only) deeper volume transport anomalies.

If the wind-driven enhancement to the NADW cell is purely a consequence of the zonal periodicity of the channel, wind anomalies immediately north of the channel should not affect the large-scale NADW cell strength. This is tested with the Channel Wind experiment (see section 3). As Fig. 6 shows, the anomaly is somewhat weaker than the Strong Wind anomaly. The difference in overturning between Strong Wind and Channel Wind experiments (Fig. 7) shows that the wind north of the channel is associated with an overturning cell that stretches across the basin to the northern boundary, with the Ekman flow continuing northward in the upper 500 m (presumably as geostrophic flow) and returning principally between 500 and 1500 m. The layer model shows a similar result, but with Ekman return flow somewhat deeper (1–3 km) and cross-equatorial flow somewhat larger. The Strong-minus-Channel overturning difference is less isopycnal than the differences between either Strong or Channel Wind experiments and the Weak Wind experiments, as witnessed by the vertically running streamlines away from the outcrop latitudes in Fig. 7.

Comparison of the Channel Wind, Strong Wind, and Weak Wind experiments indicate that a windstress perturbation in one hemisphere of a two-hemisphere ocean leads to basin-wide overturning anomaly even when the perturbation is not in a latitude belt in which the basin is zonally periodic. To further explore this behavior, we conduct the Northern Wind experiment, in which the winds north of 30°N are enhanced relative to the Strong Winds case (see section 3 and Fig. 1). The overturning anomaly induced by this wind anomaly is similar to the Strong-minus-Channel anomaly (Fig. 7). Both show about 1 Sv or so of overturning anomaly reaching the equator, and both have anomalous cells confined to the top 1.5 km or so of the water column. These similarities exist despite the difference in the wind perturbations and the difference in which hemisphere is being perturbed. Dynamically, the Northern Hemisphere differs from the southern not only in geometry but also in having the sinking limb of the NADW cell. In the layer model, the Strong-minus-North overturning is somewhat weaker and does not show near antisymmetry with the Strong-minus-Channel anomaly.

For a clearer measure of how meridional volume transport anomaly varies with latitude, we take the difference in $\Phi_z(\phi, z)$ between two runs and then find the maximum value at each ϕ. We calculate this for both total overturning and for the advective component only; for a given pair of experiments, we compare them to the Ekman volume transport anomaly implied by the difference in wind stress between the two experiments (Fig. 8). For all the pairs of experiments shown, the advective volume transport anomaly is close to that predicted by Ekman theory in the region of strongest wind anomaly. In these regions, the eddy component associated with the GM mixing tends to counteract the wind-induced transport so that the total overturning anomaly is significantly less than the advective component. Away

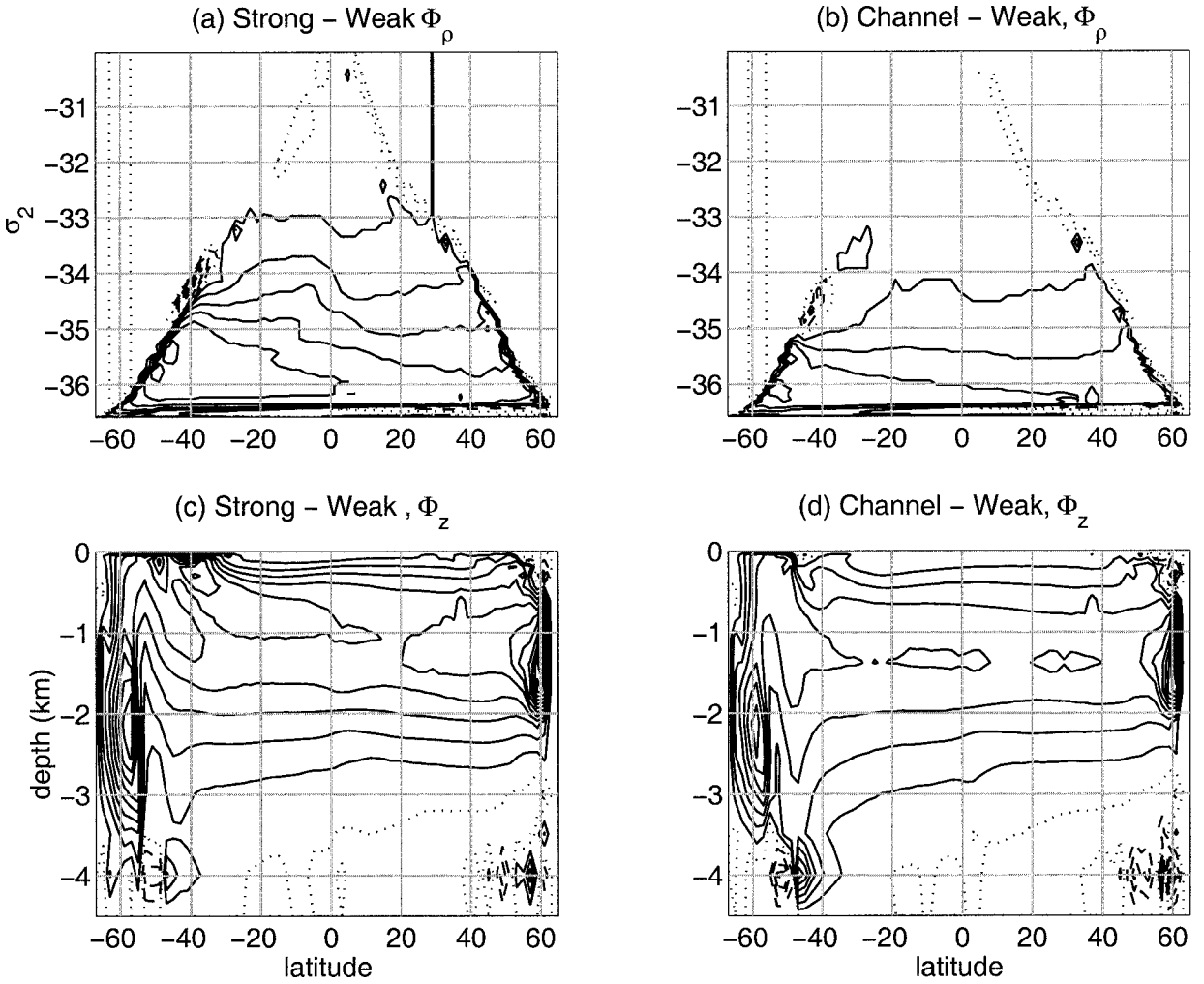

FIG. 6. Difference in (top) Φ_ρ and in (bottom) Φ_z between (left) Strong Wind and Weak Wind GM experiments and (right) Channel Wind and Weak Wind experiments. Contour interval is 0.5 Sv.

from the wind perturbation regions, all pairs of runs have significant volume transport anomalies (both total and advective components).

How strongly the wind stress just north of the channel influences volume transport throughout the basin appears somewhat different depending on exactly which runs are compared. The volume transport anomaly relative to the Weak Wind experiment is about 0.5 Sv greater at the equator in the Strong Wind run than in the Channel Wind run (Figs. 8a,b). However, the difference between the Strong Wind and Channel Wind runs shows about 1 Sv at the equator. This is because the streamfunction anomaly associated with the wind north of the Channel is not as deep as the anomaly associated with the wind south of the channel. In Φ_ρ, the difference between Strong-minus-Weak and Channel-minus-Weak is also somewhat greater, with the former about 50% greater than the latter at the equator.

b. Heat transport

Just as important as the meridional overturning in the ocean is the meridional heat transport occurring there. Therefore it is useful to explain how the heat transport depends on the forcing. The key contributors to the large scale meridional heat transport are the shallow subtropical cells driven by the tropical easterlies, the meridional overturning associated with vertical mixing (principally the NADW cell as well as a shallower cell in the Southern Hemisphere), and the perturbation to the NADW cell caused by the midlatitude westerly winds. By comparing the different experiments, we can analyze the contribution of each mechanism. We will review all the contributions and show how the contributions due to κ_V and the westerlies can be predicted from minimal assumptions.

In the discussion below, heat transport includes advection, horizontal diffusion, and bolus velocity terms;

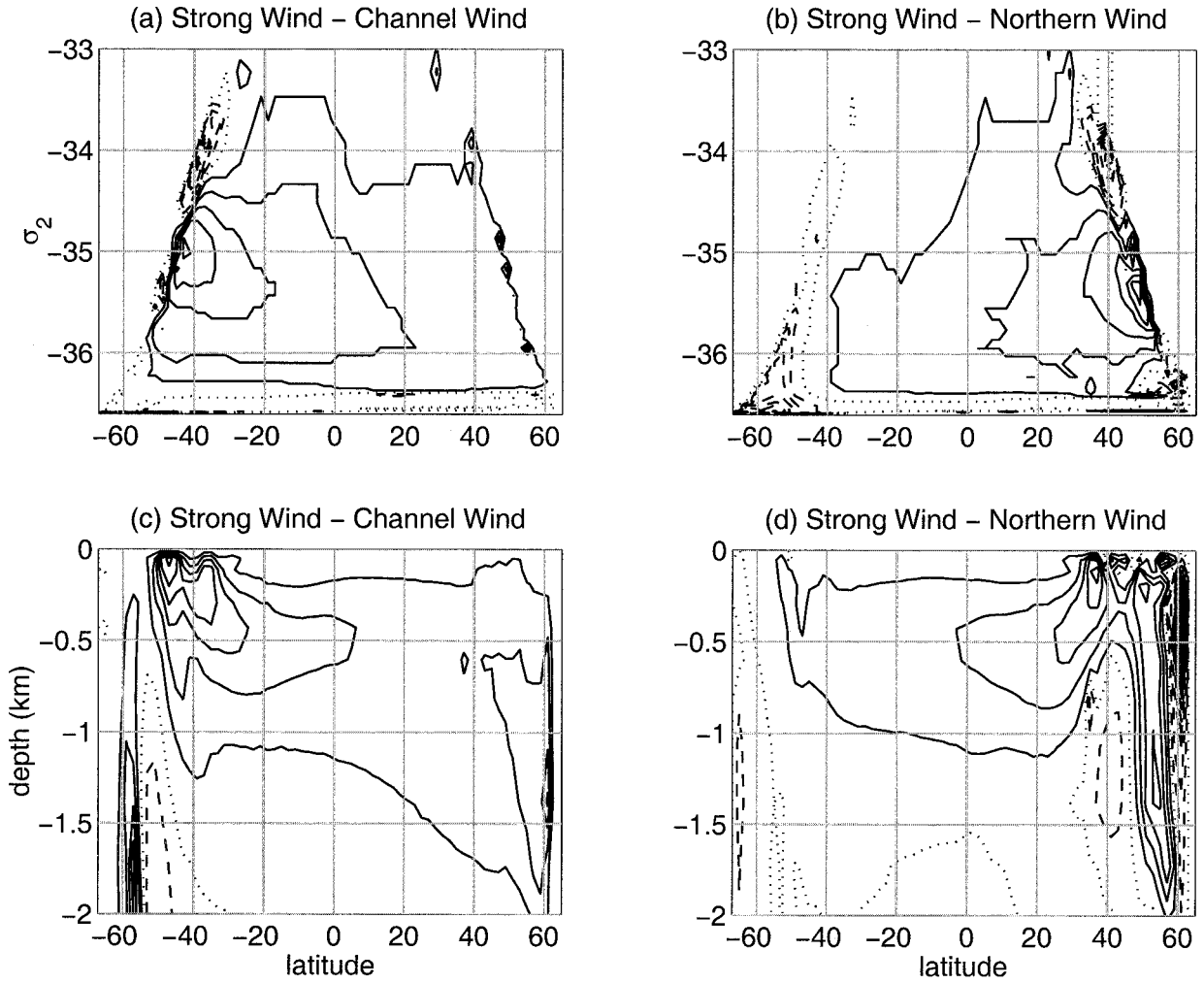

FIG. 7. Difference in (top) Φ_ρ and in (bottom) Φ_z between (left) Strong Wind and Channel Wind GM experiments and (right) Strong Wind and Northern Wind experiments. Contour interval is 0.5.

except at high latitudes it is dominated by advection. The I experiments do not calculate separate S and T fields but only ρ so that, strictly speaking, only the density transport, rather than the heat transport, can be calculated. To estimate the heat transport that the layer model would have if driven by separate S and T forcing, we use the T–S relationship from the surface forcing of the level model to calculate a $T(\rho)$ in the layer model.

In all experiments, there is at least some poleward heat transport in both hemispheres (Fig. 9a). In most of the experiments, the heat transport is much greater in the Northern Hemisphere than in the Southern, reflecting the equatorial asymmetry of the NADW cell. Despite their relatively large volume transports, the H experiments (not shown) transport about the same amount of heat as the GM and I experiments (Fig. 9a). This is partly because most of the difference in overturning occurs close to where the water sinks. Differences in heat transport, discussed below, are also similar for GM, H, and I experiments.

The subtropical cells are highlighted by the Weak Wind, Low-κ_V experiment (Fig. 2, lower-left panel), in which all the other overturning circulations are weak. Klinger and Marotzke (2000) discuss a simple expression for heat transport based on the Ekman transport and the surface temperature distribution.

When κ_V is increased, the additional meridional heat transport is poleward over most of the domain in both hemispheres (Fig. 9b). The change is stronger in the Northern Hemisphere, where the thermohaline overturning is stronger than in the Southern Hemisphere.

The heat transport associated with the classical diffusively driven, single hemisphere overturning has also been discussed in the context of box models (e.g., Nakamura et al. 1994; Marotzke and Stone 1995). Poleward heat transport is approximately given by

$$Q(\phi) = 0.5 c_p \rho \Phi_{\max}(\phi)[T_S(\phi) - T_S(\phi_0)], \quad (17)$$

where $c_p = 4.1 \times 10^3$ J kg^{-1} C^{-1} is the specific heat, $\rho = 1025$ kg m^{-3} is a typical density, T_S is the surface

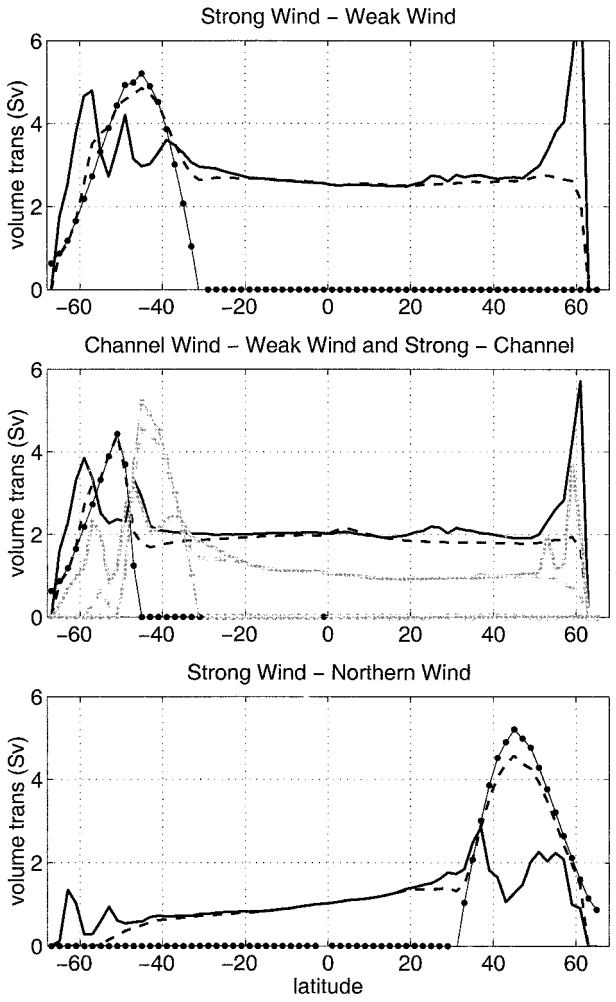

FIG. 8. Meridional volume transport $\Phi_z(\phi)$ anomaly (as measured by the maximum at each latitude) for advective plus eddy component of velocity (solid line) and for advective velocity only (dashed line), GM experiments. Ekman transport predicted by difference in wind stress is also shown (dotted line). (a) Strong Wind minus Weak Wind runs; (b) Channel Wind minus Weak Wind runs (dark) and Strong Wind minus Channel Wind runs (light); and (c) Strong Wind minus Northern Wind runs.

temperature, and ϕ_0 is the latitude where the water sinks. The case of two hemispheres is more complicated, and it is difficult to derive a simple expression for the heat transport in the Southern Hemisphere where both the ''subordinate'' and NADW cells are active. The change in Northern Hemisphere heat transport (Fig. 9b) is approximately accounted for by (17). Again, we omit details of this calculation.

Increasing the wind south of 30°S drives a northward heat transport anomaly at almost all latitudes (Fig. 9b). The anomalous density transformation poleward of latitude 30° (see previous subsection) is reflected in the heat transport anomaly (Fig. 9b), which shows large gradients (indicating surface heat flux) there. Hasumi and Suginohara (1999) found similar heat flux anomalies for a global model.

Wind anomalies outside the channel have a more pronounced influence on the meridional heat transport than on the volume transport. The Channel Wind heat transport anomaly (relative to Low Wind case) is only about half as strong as the Strong Wind heat transport anomaly, while the Northern Wind heat transport anomaly (relative to Strong Wind case) is of similar magnitude to the Channel Wind anomaly (Fig. 9b). We can estimate the heat transport anomaly from the temperature and volume transport scales involved. If the overturning circulation anomaly has characteristic volume transport ΦA and characteristic temperature difference ΔT between northward- and southward-flowing limbs of the cell, then the heat transport Q is given by

$$Q = c_p \rho \Delta T \Phi_A. \tag{18}$$

In the previous subsection, we discussed the variations in Φ caused by the wind, but we also need to estimate ΔT. If the subsurface temperature changes of a water parcel are small compared to the temperature changes at the surface, then ΔT should be given by the temperature difference between the water upwelling into the Ekman layer and the water downwelling from the Ekman layer (Klinger and Marotzke 2000). To put it another way, the heat transport at the equator due to wind stress far to the south is due to northern flow of warm water with temperature characteristic of Ekman downwelling north of the channel and to southern flow of cold water with a temperature characteristic of Ekman upwelling south of the channel. Here we approximate the average downwelling temperature by the restoring temperature at the latitude midway between the maximum and zero values of Ekman transport anomaly. For the Strong Wind case, that temperature difference is given by the SST difference between the southern edge of the channel and 40°S. For the Channel Wind case, the water should downwell at 48°S instead of 30°S. We can even include the Northern Wind case, by simply taking the temperature difference between 64°N and 38°N.

Table 4 compares estimates to actual values of equatorial heat transport anomaly for each experiment. The Φ_A values are taken from Φ_z differences from the numerical experiment, so the accuracy of the estimate is really a test of the sensitivity of the heat transport to the estimated temperature range. The table shows that all the heat transport estimates are within about 15% of the actual values for the numerical experiments.

c. Diabatic flow and three-dimensional circulation

Despite the success of the above analysis in predicting the heat transport due to changes in the westerlies, it would be misleading to think that there is no diabatic circulation induced outside the density range that is ventilated in the latitude range of the wind anomaly. The

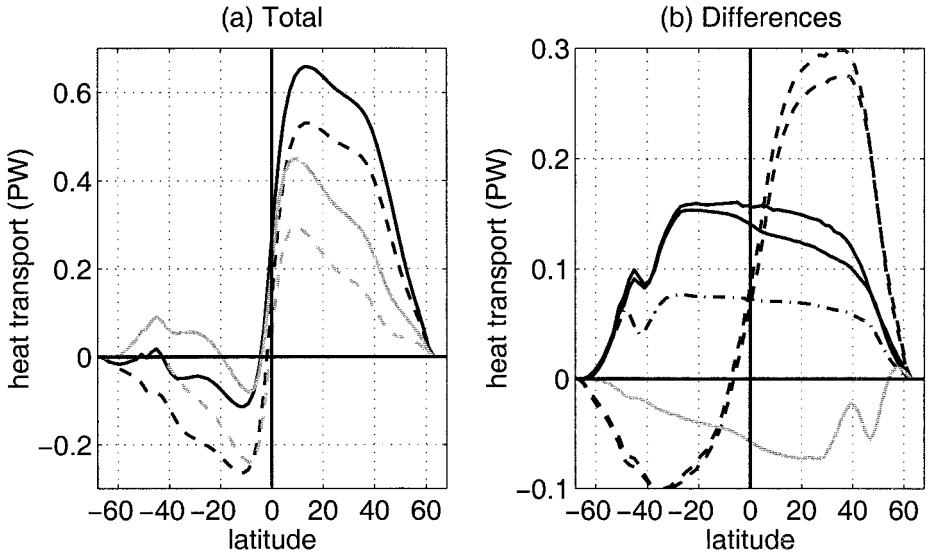

FIG. 9. (a) Meridional heat transport as a function of latitude for GM experiments, for strong wind (solid lines), weak wind (dashed lines), high κ_V (black), and low κ_V (gray). (b) Differences in heat transport for GM experiments due to changes in τ south of 30°S (dark solid), κ_V (dashed), τ over the channel only (dash–dot), and τ north of 30°N (gray solid).

streamlines in Fig. 6 give the impression that all the flow pushed into the Northern Hemisphere by the Ekman transport anomaly dives below the surface at the northern edge of the wind anomaly. In reality, there is a surface circulation anomaly throughout the entire basin for both the strong wind and channel wind anomalies (Fig. 10). In both cases, a western boundary current anomaly flows from about 30°S to the basin's northern boundary. For the Channel Wind anomaly, there is an anomalous surface gyre north of the wind anomaly. This gyre is also visible in Fig. 7 because there is a density difference between the northward western boundary flow and the southward ''interior'' flow, but Fig. 10 shows that the western boundary flow actually continues northward through the entire basin.

Thus we see two views of the induced circulation pattern: the upper limb of the cell seems to approximately follow isopycnals, but some flow remains confined to the surface where it can cross isopycnals under the influence of surface heating and cooling. This raises the question of how much of the flow actually follows the isopycnal path. We obtain a rough measure of this by calculating the zonal average meridional velocity anomaly $v_A(\phi, z)$ from $\Phi_z(\phi, z)$. For the Strong Wind anomaly, at 25°S, v_A is almost as large at the surface as its peak value deeper in the water column, which is at depth about 200 m. For the Channel Wind anomaly, at 25°S, the surface v_A is only about half its peak value. By 15°S, however, the surface v_A is about half its peak value for both runs, and at 5°S it has further decreased to about one third the peak value for the Strong Wind anomaly. In summary, most of the induced flow approximately follows isopycnals, but there is substantial flow that is lighter and warmer than any that was pumped down in the region of wind anomaly.

TABLE 4. Estimated and actual equatorial heat transport anomaly: ΔT (°C), Φ_A (Sv), Q_{est} (estimated equatorial heat transport) and Q_{act} (actual equatorial heat transport) (PW).

Run	ΔT	Φ_A	Q_{est}	Q_{act}
Strong–Weak	12.3	2.5	0.13	0.14
Channel–Weak	7.5	2.0	0.063	0.072
Strong–Northern	13.5	1.0	0.057	0.057

6. Conclusions

We have used numerical models with different parameterizations of eddy mixing of density [horizontal (H) and isopycnal/Gent–McWilliams (GM)] and different discretizations [level and layer (I)] to study the sensitivity of an idealized Atlantic basin to vertical mixing and basin width and to wind strength over a zonal subpolar channel analogous to earth's Southern Ocean. For all versions of the experiments, increases in diapycnal mixing or subpolar wind stress increase the strength of the model's version of the North Atlantic Deep Water (NADW) meridional overturning cell. There are quantitative differences between the different mixing and numerical schemes. In particular, H has larger overturning than GM because of the greater diapycnal mixing associated with horizontal mixing. GM, in turn, has slightly larger overturning than I, presumably due to level-model numerics being more diffusive.

Gnanadesikan (1999) derived a cubic equation that describes the strength of the NADW cell. We nondimensionalize this cubic and derive a simplified, closed-form expression for the resulting scaling. The expression re-

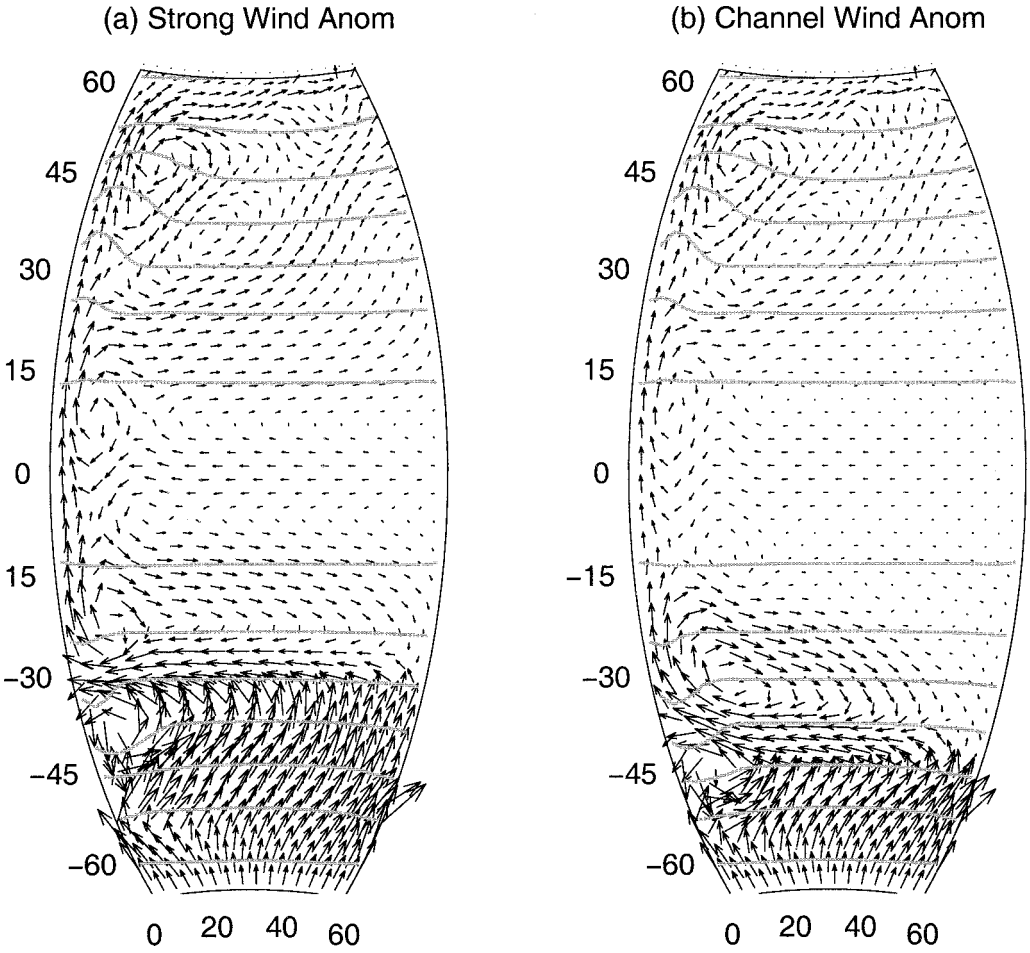

FIG. 10. Surface-level (depth 25 m) velocity anomaly relative to Weak Wind experiment for (a) Strong Wind and (b) Channel Wind experiments. Arrow lengths are proportional to square root of speed so that both weak and strong flows can be easily seen. Alternate grid points are removed to reduce clutter in the figure. Contours show surface level temperature with contour interval of 4°C.

lates the pycnocline depth and overturning strength to the classical advective–diffusive scales for these quantities and to nondimensional external parameters representing the Ekman transport and thickness diffusion in the Southern Ocean. The relative importance of the wind-stress and vertical mixing for driving deep meridional overturning in the real world depends on some large-scale average of vertical eddy diffusivity, κ_V, which is difficult to measure. Our analysis of the scaling implies that the κ_V must be less than about 0.1 cm^2 s^{-1} for wind stress to make overturning at least 50% greater than what it would be if driven by mixing alone.

The Gnanadesikan scaling only roughly fits the H experiments but provides a fairly good fit to the experiments with isopycnal/GM mixing (experiments GM and I).

We show that enhanced Southern Ocean westerlies drive an overturning anomaly in the form of a basinwide cell connecting Southern Ocean upwelling and downwelling near the northern boundary of the basin, consistent with the Toggweiler and Samuels (1995) conclusions based on total (as opposed to anomaly) overturning. The anomalies may be relevant to oceanic variability since variability in the mean westerlies may drive similar anomalies in the ocean. Wind stress fluctuations, as a fraction of the time mean, are likely to be weaker than is imposed in our experiments, but the wider zonal extent of the real Southern Ocean might allow such wind-induced overturning variability to be measurable.

Despite the success of the G99 scaling, several factors controlling the NADW cell strength are outside the scope of the G99 scaling. In particular, the G99 scaling and Toggweiler and Samuels' (1995) original description does not take into account wind outside the Southern Ocean channel. In contrast, Tsujino and Suginohara (1999) find that wind stress applied to one hemisphere of a basin with *no channel* also has a strong effect on the deep overturning cell. In our experiments, wind perturbations just north of the channel or north of 30°N produce basinwide circulation anomalies that are shal-

lower than anomalies induced by similar windstress perturbations in the Channel, with volume transport about 1/3 as strong and heat transport anomalies about half as strong. To summarize, we find that winds outside the channel have a significant basinwide influence, but not as strong as implied by the experiments of Tsujino and Suginohara (1999), in which less of the subpolar meridional Ekman transport returns locally and more makes the basin-wide circuit. We analyze the differences between their experiments and ours in a forthcoming paper.

Previous studies have explained how the magnitude of heat transport follows from the overturning circulation associated with the trade winds and the mixing-driven NADW cell. Here we separate the total heat transport into components associated with these processes as well as a component due to midlatitude westerlies. We then estimate the heat transport due to the westerlies based on the volume transport anomaly and externally imposed surface temperature. By assuming that the anomalous Ekman pumping that flows across the equator follows an approximately isopycnal path, we make fairly accurate predictions of the heat transport driven by wind both inside the channel latitudes and outside. However, closer examination of the velocity anomaly shows that there is also a surface western boundary current anomaly flowing from the wind perturbation region to the equator and beyond. In our experiments, near the equator the surface component is about 1/3 as strong as the isopycnal component. However, it is not clear what controls the proportion of the cross-equatorial flow that follows the surface path, and this proportion may be different in different experimental configurations, such as one with a more intense (and realistic) western boundary current.

Acknowledgments. Barry Klinger was supported by NSF Grant OCE-9730554 at NSU and OCE-0196117 at GMU. Elena Boguslavsky and Kevin Kohler gave computer assistance. Thanks go to Paul Schopf for some interesting discussion, and to two anonymous reviewers for their detailed comments.

APPENDIX

Resolution Sensitivity

Numerical experiments are repeated with different horizontal resolution but with all other parameters [including horizontal viscosity, which controls western boundary current (WBC) width] identical. As Table A1 shows, overturning strengths are somewhat higher at $4° \times 3.75°$ resolution, than with $2° \times 2°$ resolution. The H experiments are much more sensitive to resolution than the GM experiments. For the layer model, the sensitivity to resolution is higher for weak diapcynal mixing. In that case, the water mass transformation is dominated by buoyancy change at the surface, which is treated differently in the layer model. A velocity section through the WBC of the high-κ_V, low-wind GM case shows that the current is the same width at both resolutions, indicating that even at coarse resolution the grid is resolving the WBC. Nevertheless, only about two grid points are included in the WBC at coarse resolution. This may be especially problematic because of the flux-corrected transport scheme we use, which can introduce a significant amount of numerical diffusivity in temperature structures that are just barely resolved by the grid (Griffies et al. 2000).

Further high-κ_V, low-wind experiments at $1° \times 1°$ resolution improve our knowledge of how well the numerical experiments approximate the continuous problem (see Table A2). Linearly extrapolating the 2° and 1° experiments to estimate the ''infinite resolution'' solution (Table A2), we find that for GM mixing, even $4° \times 3.75°$ resolution gives overturning that is less than 10% greater than the estimated infinite resolution solution. In H mixing experiments, numerical errors are leading order at $4° \times 3.75°$, and even 1° resolution may have significant errors. At all resolutions, the H experiment has greater NADW cell volume transport than the corresponding GM experiment. While GM experiments take about twice as much computer time as corresponding H experiments, for a given WBC width, the GM parameterization may actually demand less computer time because not as high horizontal resolution is required.

The ratio of H overturning to GM overturning increases linearly with grid spacing. At 3.75°, the overturning is 1.8 to 2.5 times greater for H than for corresponding GM experiments. For the 0° extrapolation, H is only 1.1 to 1.7 times greater than GM (generally a smaller ratio for higher κ_V).

TABLE A1. Comparison of low-resolution and high-resolution overturning for low and high winds: κ_V as in Table 1; numbers refer to NADW peak volume transport in ρ coordinates; and ''ratio'' (nondimensional) refers to low-resolution values divided by high-resolution values.

	H (level model)		GM (level model)		Layer model	
κ_V	Low	High	Low	High	Low	High
0.05 (ratio)	1.18	1.34	1.00	1.15	1.46	1.35
0.50 (ratio)	1.30	1.26	1.07	1.12	1.12	1.11

TABLE A2. Overturning as a function of resolution. Overturning is ρ-coordinate NADW volume transport (Sv) for 1° resolution experiments and extrapolation to 0° resolution. Overturning ratio is volume transport normalized by 0° estimate.

	Overturning		Overturning ratio		
Mixing	1°	0°	1°	2°	3.75°
H	12.0	10.4	1.15	1.31	1.70
GM	9.1	9.0	1.01	1.02	1.09

REFERENCES

Bleck, R., and D. B. Boudra, 1986: Wind driven spin-up in eddy-resolving ocean models formulated in isopycnic and isobaric coordinates. *J. Geophys. Res.,* **91,** 7611–7621.

——, and L. T. Smith, 1990: A wind-driven isopycnic coordinate model of the North and equatorial Atlantic Ocean. 1. Model development and supporting experiments. *J. Geophys. Res.,* **95,** 3273–3285.

Böning, C. W., W. R. Holland, F. O. Bryan, G. Danabasoglu, and J. C. McWilliams, 1995: An overlooked problem in model simulations of the thermohaline circulation and heat transport in the Atlantic Ocean. *J. Climate,* **8,** 515–523.

Bryan, F., 1987: Parameter sensitivity of primitive equation ocean general circulation models. *J. Phys. Oceanogr.,* **17,** 970–985.

Bryan, K., 1984: Accelerating the convergence to equilibrium of ocean-climate models. *J. Phys. Oceanogr.,* **14,** 666–673.

——, and M. D. Cox, 1967: A numerical investigation of the oceanic general circulation. *Tellus,* **19,** 54–80.

Colin de Verdiere, A., 1988: Buoyancy driven planetary flows. *J. Mar. Res.,* **46,** 215–265.

Cox, M. D., 1989: An idealized model of the World Ocean. Part I: The global-scale water masses. *J. Phys. Oceanogr.,* **19,** 1730–1752.

Danabasoglu, G., and J. C. McWilliams, 1995: Sensitivity of the global ocean circulation to parameterization of mesoscale tracer transports. *J. Climate,* **8,** 2967–2987.

——, ——, and P. R. Gent, 1994: The role of mesoscale tracer transports in the global ocean circulation. *Science,* **264,** 1123–1126.

Drijfhout, S. S., 1994: On the heat transport by mesoscale eddies in an ocean circulation model. *J. Phys. Oceanogr.,* **24,** 429–442.

Gent, P. R., and J. C. McWilliams, 1990: Isopycnal mixing in ocean circulation models. *J. Phys. Oceanogr.,* **20,** 150–155.

Gerdes, R., C. Koberle, and J. Willebrand, 1991: The influence of numerical advection schemes on the results of ocean general circulation models. *Climate Dyn.,* **5,** 211–226.

Gnanadesikan, A., 1999: A simple predictive model for the structure of the oceanic pycnocline. *Science,* **283,** 2077–2079.

Gregg, M. C., 1987: Diapycnal mixing in the thermocline: A review. *J. Geophys. Res.,* **92,** 5249–5286.

Griffies, S. M., R. C. Pacanowski, and R. W. Hallberg, 2000: Spurious diapycnal mixing associated with advection in a z-coordinate ocean model. *Mon. Wea. Rev.,* **128,** 538–564.

Hasumi, H., and N. Suginohara, 1999: Atlantic deep circulation controlled by heating in the Southern Ocean. *Geophys. Res. Lett.,* **26,** 1873–1876.

Hellerman, S., and M. Rosenstein, 1983: Normal monthly wind stress over the world ocean with error estimates. *J. Phys. Oceanogr.,* **13,** 1093–1104.

Hirst, A. C., and T. J. McDougall, 1998: Meridional overturning and dianeutral transport in a z-coordinate ocean model including eddy-induced advection. *J. Phys. Oceanogr.,* **28,** 1205–1223.

——, D. R. Jackett, and T. J. McDougall, 1996: The meridional overturning cells of a World Ocean model in neutral density coordinates. *J. Phys. Oceanogr.,* **26,** 775–791.

Huang, R. X., and K. Bryan, 1987: A multilayer model of the thermohaline and wind-driven ocean circulation. *J. Phys. Oceanogr.,* **17,** 1909–1924.

Klinger, B. A., 2000: Acceleration of general circulation model convergence by exponential extrapolation. *Ocean Modell.,* **2,** 61–72.

——, and J. Marotzke, 1999: Behavior of double hemisphere thermohaline flows in a single basin. *J. Phys. Oceanogr.,* **29,** 382–399.

——, and ——, 2000: Meridional heat transport by the subtropical cell. *J. Phys. Oceanogr.,* **30,** 696–705.

Ledwell, J. R., A. J. Watson, and C. S. Law, 1993: Evidence for slow mixing across the pycnocline from an open-ocean tracer-release experiment. *Nature,* **365,** 701–703.

Marotzke, J., 1997: Boundary mixing and the dynamics of three-dimensional thermohaline circulations. *J. Phys. Oceanogr.,* **27,** 1713–1728.

——, and P. H. Stone, 1995: Atmospheric transports, the thermohaline circulation, and flux adjustments in a simple coupled model. *J. Phys. Oceanogr.,* **25,** 1350–1364.

——, and B. A. Klinger, 2000: Dynamics of equatorially asymmetric thermohaline circulations. *J. Phys. Oceanogr.,* **30,** 950–970.

McCreary, J., and P. Lu, 1994: Interaction between the subtropical and equatorial ocean circulations: The subtropical cell. *J. Phys. Oceanogr.,* **24,** 466–497.

McDermott, D. A., 1996: The regulation of northern overturning by Southern Hemisphere winds. *J. Phys. Oceanogr.,* **26,** 1234–1255.

McDougall, T. J., 1987: Neutral surfaces. *J. Phys. Oceanogr.,* **17,** 898–942.

Nakamura, M., P. H. Stone, and J. Marotzke, 1994: Destabilization of the thermohaline circulation by atmospheric eddy transports. *J. Climate,* **7,** 1870–1882.

Pacanowski, R. C., 1996: MOM 2 version 2.0 (Beta) documentation user's guide and reference manual. GFDL Ocean Tech. Rep. 3.2, 329 pp.

Park, Y.-G., and K. Bryan, 2000: Comparison of thermally driven circulations from a depth coordinate model and an isopycnal layer mode. Part I: A scaling law—Sensitivity to vertical diffusivity. *J. Phys. Oceanogr.,* **30,** 590–605.

Polzin, K., J. Toole, J. Ledwell, and R. Schmitt, 1997: Spatial variability of turbulent mixing in the abyssal ocean. *Science,* **276,** 93–96.

Rahmstorf, S., 1996: On the freshwater forcing and transport of the Atlantic thermohaline circulation. *Climate Dyn.,* **12,** 799–811.

——, and M. H. England, 1997: Influence of Southern Hemisphere winds on North Atlantic Deep Water flow. *J. Phys. Oceanogr.,* **27,** 2040–2054.

Scott, J. R., 2000: The roles of geothermal heating, diapycnal mixing, and surface bouyancy forcing in meridional overturning dynamics. Ph.D. thesis, Massachusetts Institute of Technology, 128 pp.

Toggweiler, J. R., and B. Samuels, 1995: Effect of Drake Passage on the global thermohalinel circulation. *Deep-Sea Res.,* **42,** 477–500.

——, and ——, 1998: On the ocean's large-scale circulation near the limit of no vertical mixing. *J. Phys. Oceanogr.,* **28,** 1832–1852.

Toole, J., R. Schmitt, K. Polzin, and E. Kunze, 1997: Fine and microstructure evidence of boundary mixing above the flanks of a mid-latitude seamount. *J. Geophys. Res.,* **102,** 947–959.

Tsujino, H., and N. Suginohara, 1999: Thermohaline circulation enhanced by wind forcing. *J. Phys. Oceanogr.,* **29,** 1506–1516.

Veronis, G., 1975: The role of models in tracer studies. *Numerical Models of the Ocean Circulation,* Nat. Acad. Sci., 133–146.